Environmental Science and Pollution Research (2023) 30:114484–114500
https://doi.org/10.1007/s11356-023-30286-1

RESEARCH ARTICLE

CFD-based simulation study of dust transport law and air age in tunnel under different ventilation methods

Wen Nie[1,2] · Chenwang Jiang[1,2] · Ning Sun[1,2] · Lidian Guo[1,2] · Qiang Liu[1,2] · Chengyi Liu[1,2] · Wenjin Niu[1,2]

Received: 19 April 2023 / Accepted: 2 October 2023 / Published online: 20 October 2023

Abstract
To solve the problem of high-concentration dust pollution in a bored tunnel, we conducted a simulation study on the dust transport law and air age of the wind flow in a bored tunnel under different ventilation methods. Air age was innovatively introduced as an index for evaluating tunnel air quality. The results show that dust pollution is serious under conditions of press-in ventilation, which is unfavorable to personnel operations. Following the installation of an on-board dust-removal fan, an effective dust-control air curtain forms in the tunnel, and the high-concentration dust is essentially controlled within the range of $Z = 13$ m from the working face. The dust concentration in the working area on the left side of the tunnel is $C_D < 200$ mg/m^3, and the dust-control effect is obvious. At the same time, the air age on both sides of the tunnel is reduced by 35.5% following the use of the on-board dust-removal fan. Taking into account dust control by ventilation and dust removal by fan, spraying dust reduction measures are added, and we developed automated wind-mist synergistic wet high-frequency oscillation dust-capturing technology for tunnel boring. This could effectively improve the problem of high levels of coal dust pollution in tunnels.

Keywords Production environment · Dust control effect · Numerical simulation · Air age in tunnel

Introduction

According to the Statistical Review of World Energy Resources of 2019, the world coal output in 2018 was 8.01 billion tons, which corresponds to an increase of 4% over 2017. China's coal production accounts for 46% of the production worldwide, which corresponds to an increase of 0.4% compared to 2017. Evidently, coal will keep an important position in the energy consumption structure for a considerable period. Owing to the development of society, science, and technology, the speed and efficiency of coal mining have been improved. However, even more coal dust is created during operations in coal mine tunnels (Azam and Mishra 2019; Xiao et al. 2022; Lu et al. 2021). It pollutes the working environment and is the main cause of pneumoconiosis in China. By the end of 2018, a total of 23,497 cases of occupational diseases had been reported, including 19,468 cases of occupational pneumoconiosis; they account for 82.9% of the total number of occupational disease cases, of which more than 90% were coal miners suffering from pneumoconiosis (Feng et al. 2022; Wang et al. 2019; Zhang et al. 2021). Therefore, the working environment in coal mines during excavations must be improved, and the health of workers must be protected.

To improve the working environment in coal mine tunnels, scholars from different countries have studied the airflow and dust transport during operations in tunnels. For example, Laín and Sommerfeld compared the characteristics of gas–solid multiphase fluids in pipes of different lengths, degrees of roughness, and angles with the Euler–Lagrangian method (Laín and Sommerfeld 2012). Rao et al. simulated airflow and dust migration during operations in tunnels (Xie et al. 2018). In addition, Fang et al. studied the effect of the distance between the air duct outlet and the working face on the airflow and dust during the construction of a highway

Responsible Editor: Marcus Schulz

✉ Lidian Guo
sdustguold@163.com

[1] College of Safety and Environmental Engineering, Shandong University of Science and Technology, Shandong Province, Qingdao 266590, China

[2] State Key Laboratory of Mining Disaster Prevention and Control Co-Found By Shandong Province and the Ministry of Science and Technology, Shandong University of Science and Technology, Qingdao 266590, China

tunnel (Zhuo et al. 2021; Zhang et al. 2019). Using CFD software, Toraño et al. studied the change in the air speed and dust concentration in each section of a tunnel with press-in ventilation (the main ventilator pressed fresh air into the area of the working face) and far-pressing-near-absorption (FPNA) ventilation (Toraño et al. 2011). Nie et al. simulated the effect of airflow inlet points and the exhaust air rate on dust control under FPNA ventilation in long-distance and large-section tunnels (Nie et al. 2022). Moreover, Li et al. verified the effectiveness of a wall-attached swirl ventilation device through Fluent simulations. When the width and length of the strip-shaped airflow outlet increase, the dust concentration at the position of the tunneling machine driver first decreases and then increases; the researchers concluded that a shaft diameter–exhaust air rate ratio of 2:8 is most effective within the ventilation safety limit. The authors also verified the reliability of the simulation data (Li et al. 2020). Finally, Wang et al. used lightweight polymer materials to build a multi-radial dust-controlling air curtain device and performed simulations with the k-ε model. They discovered that the larger the radial diffusion is, the better it promotes the formation of a dust-controlling air curtain. The authors also determined the most effective exhaust air rate and shaft diameter–exhaust air rate ratio (Wang et al. 2018).

The air age refers to the age of an air proton, i.e., the time that an air proton takes to travel from an inlet point to the measurement point (Hongchao et al. 2019; Kwon et al. 2011). It reflects the air freshness and, therefore, comprehensively represents the ventilation effect in a space (Ding et al. 2019; Hu et al. 2020). To the best of our knowledge, researchers have always studied the air age in buildings and indoor thermal environments. For example, Buratti et al. used the CO_2 tracer gas concentration attenuation method to evaluate the average air age in an office. They concluded that the air quality is best when the doors and windows are open and four different natural ventilation methods are applied. In addition, the air quality is related to the season and temperature (Buratti et al. 2011). Mao et al. studied the effect of airflow outlet heights on the average air age distribution, CO_2 concentration distribution, and ventilation efficiency in a sleep environment. Their results showed that a lower airflow outlet saves energy and improves the breathing environment (Ning et al. 2016). Furthermore, Park et al. numerically simulated the average air age to study the effect of mesh numbers on the effect of press-in ventilation. They also investigated the effects of the air velocity, air duct angle, and distance from the pressure inlet to the cutting face on the air quality in a tunnel (Park et al. 2018).

Although researchers have achieved good results, the following deficiencies must be addressed: (1) the physical model used in the published research studies is relatively simple, which results in large deviations between the simulation results and actual conditions; (2) the airflow and dust created by a roadheader with an on-board dust fan in a coal mine tunnel have not been thoroughly investigated; and (3) there is no reasonable index for evaluating the air quality in tunnels for the prevention and control of coal dust pollution. Therefore, the topic of this study is the coal dust pollution law in tunnels with different ventilation modes. First, a 1:1 isometric model was built with SOLIDWORKS based on field investigations, and Fluent was used to study the distribution of the airflow field and dust transport in tunnels with press-in ventilation and an additional on-board dust fan. The air age was innovatively introduced as an evaluation index for the air quality in a tunnel to study its changes under different ventilation methods. In addition to dust control through ventilation and dust removal through the fan, the dust concentration was reduced via spraying. Therefore, an automatic wind-mist synergistic wet high-frequency oscillation dust-capturing technology for tunnel boring processes was developed. The research method and results enrich the theory of dust pollution prevention and control during tunnel boring; they can provide new ideas for evaluating the degrees of coal dust pollution and the air quality during tunnel boring.

Physical and mathematical models

Selection of mathematical models

The migration of a fluid can be described with the Euler–Lagrangian method, and the airflow in a tunnel follows the basic law of fluid mechanics (Bayatian et al. 2021; Chang et al. 2020; Liu et al. 2022; Morozova et al. 2022). For the simulation of the airflow, the realizable k-ε model was used to include the gas–solid coupling equation (de Medeiros Lima et al. 2021; Korkmaz et al. 2021; Li et al. 2023; Wang et al. 2021).

The continuity equation for the gas phase is as follows:

$$\frac{\partial U}{\partial x}+\frac{\partial V}{\partial y}+\frac{\partial W}{\partial z}=0 \tag{1}$$

The momentum equation for the gas phase is expressed as follows:

$$\frac{\partial U_i}{\partial t}+U_j\frac{\partial U_i}{\partial xj}=-\frac{1}{\rho}\frac{\partial P}{\partial xi}+v\frac{\partial^2 U_i}{\partial xi\partial xj}+\frac{1}{\rho}\frac{\partial(-\overline{pu_i'u_j'})}{\partial xj}-\overline{pu_i'u_j'} \tag{2}$$

In addition, the k equation (i.e., the turbulence kinetic energy equation) is used:

$$\frac{\partial(\rho k)}{\partial t}+\frac{\partial(\rho k u_i)}{\partial x_i}=\frac{\partial}{\partial x_j}\left[\left(\mu+\frac{\mu_t}{\sigma_k}\right)\right]+G_k-\rho\varepsilon \tag{3}$$

The ε equation (i.e., the turbulence energy dissipation rate equation) is as follows:

$$\frac{\partial(\rho\varepsilon)}{\partial t}+\frac{\partial(\rho\varepsilon u_i)}{\partial x_i}=\frac{\partial}{\partial x_j}\left[\left(\mu+\frac{\mu_t}{\sigma_\varepsilon}\right)\frac{\partial_k}{\partial x_j}\right]+\rho C_1 E\varepsilon-\rho C_2\frac{\varepsilon^2}{\kappa+\sqrt{v\varepsilon}} \tag{4}$$

Where $C_1=\max\left[0.43,\frac{\eta}{\eta+5}\right]$, $\eta=E\frac{\kappa}{\varepsilon}$, C_2 is a constant, $E=\sqrt{2E_{ij}E_{ij}}$, G_k represents the turbulent flow energy caused by the average velocity gradient with $G_k=\mu_t E^2$, and ∂_k and ∂_e are the turbulent Prandtl numbers of the κ and ε equations, respectively. The equation is solved with the empirical values $C_2=1.9$, $\sigma_k=1.0$, and $\sigma_e=1.2$.

$$\mu_t=\rho C_\mu\frac{k^2}{\varepsilon} \tag{5}$$

where the function C_μ is related to the average strain rate and turbulent flow field: $C_\mu=\frac{1}{A_0+A_s U^* k/\varepsilon}$; $A_0=4.0$; $A_s=\sqrt{6}\cos\varphi$; $\varphi=\frac{1}{3}\arccos\left(\sqrt{6}P\right)$; P is the power, W; $p=\frac{E_{ij}E_{jk}E_{kj}}{(E_{ij}E_{ij})^{1/2}}$, $E_{IJ}=\frac{1}{2}\left(\frac{\partial u_i}{\partial x_j}+\frac{\partial u_j}{\partial x_i}\right)$; U^* is the internal energy, J; $U^*=\sqrt{E_{ij}E_{ij}+\widetilde{e}_{ij}\widetilde{e}_{ij}}$; $e_{ij}=\overline{e}_{ij}-\varepsilon_{ijk}\omega_k$; $\widetilde{e}_{ij}=e_{ij}-2\varepsilon_{ijk}\omega_k$ is the fluid spin rate; and $\overline{e}_{ij}$ is the time-averaged rotation rate tensor observed from the reference frame with the angle ω_k. For a non-rotating flow field, $\widetilde{e}_{ij}\widetilde{e}_{ij}$ in U^* is zero in the presented non-spinning flow field; it is introduced to consider the spin effect.

To consider the characteristics of the gas–solid two-phase turbulent fluid and two-phase momentum exchange, the discrete phase model based on the Euler–Lagrange method was used in Fluent to describe dust migration (Rahimi et al. 2021; Tretiakow et al. 2021; Xu et al. 2023; Wang et al. 2020). According to the balance of forces acting on the particle, the equation in the Lagrangian coordinates is as follows (Mo et al. 2020; Sajjadi et al. 2016; Sun et al. 2021):

$$\frac{du_p}{dt}=F_D\left(u-u_p\right)+\frac{g_x\left(\rho_p-\rho\right)}{\rho_p}+F_x \tag{6}$$

where $F_D=\frac{18\mu}{\rho_p D_p^2}\frac{C_D R_e}{24}$; u is the velocity of the continuous phase; u_p is the particle phase velocity; μ is the molecular viscosity coefficient of the fluid; and ρ and ρ_p represent the density of the fluid and dust, respectively.

We assume that D_p represents the particle size with R_e:

$$R_e=\frac{\rho D_p\left|u_p-\mathrm{u}\right|}{\mu} \tag{7}$$

where the resistivity $D_p=a_1+\frac{a_2}{R_e}+\frac{a_2}{R_e^2}$ is a constant defined through experiments with smooth spherical particles; C_D can be represented as follows: $C_D=\frac{R_e}{24}\left(1+b_1 R_e b_2\right)+\frac{b_3 R_e}{b_4+R_e}$. Moreover, the shape factor can be defined as follows $\varphi=s/S$, where s is the surface area of a sphere with the same volume as a particle and S is the surface area of the particle.

The potency dimension is below the micron level, and the Stokes resistance is represented as follows:

$$F_D=\frac{18\mu}{D_p^2\rho_p C_c} \tag{8}$$

where C_c represents the Cunningham correction coefficient $C_c=1+\frac{2\lambda}{D_p}\left(1.257+0.4e^{\frac{1.1D_p}{2\lambda}}\right)$, and λ is the mean free path of a molecule.

The air age is not the residence time of air molecules in the channel at a point in that location, but the average residence time of a population of air molecules in the vicinity of that location. This group of molecules is infinitely small on the macroscopic level, with uniform temperature, humidity, and other physical properties; however, it is infinitely large on the microscopic level, embodying the statistical properties of a continuous fluid, i.e., an infinite number of microscopic particles, rather than the random movement properties of individual particles (Buratti et al. 2011; Calautit and Hughes 2014; Yuce et al. 2022).

As a result of the factors outlined above, there are air molecules of different ages in the air molecule population near the observation point of the bored tunnel, and the number of air molecules of various ages has a frequency distribution function $f(\tau)$ and a cumulative distribution function $F(\tau)$. The so-called frequency distribution function $f(\tau)$ refers to the ratio of the number of air molecules of age $\tau+\Delta\tau$ to the proportion of the total number of molecules to the ratio of $\Delta\tau$, and the cumulative distribution function $F(\tau)$ refers to the proportion of the number of air molecules of age less than τ to the proportion of the total number of molecules (Hormigos-Jimenez et al. 2018; Ning et al. 2016; Yang et al. 2014). The relationship between the cumulative distribution function and the frequency distribution function is as follows:

$$\int_0^\tau f(\tau)d\tau=F(\tau) \tag{9}$$

As the air age at a point is the average of the population of air molecules at that point, the air age τ_p at any point can be calculated from the following equation when the frequency distribution function is known.

$$\tau_p=\int_0^\infty \tau f(\tau)d\tau \tag{10}$$

Combining the N-S Eq. (11) and the mass diffusion Eq. (12)

$$\frac{\partial(\rho_1\varphi)}{\partial\tau} + \frac{\partial}{\partial x_j}(\rho_1 u_j \varphi) = \frac{\partial}{\partial x_j}\left[\Gamma_\varphi \frac{\partial\varphi}{\partial x_j}\right] + S_\varphi \tag{11}$$

$$\frac{\partial\rho_1}{\partial\tau} + \frac{\partial}{\partial x_j}(\rho_1 u_j) = \frac{\partial}{\partial x_j}\left[\Gamma_{\rho_1} \frac{\partial\rho_1}{\partial x_j}\right] + S_{\rho_1} \tag{12}$$

The steady-state case can be expressed as

$$\frac{\partial}{\partial x_j}(u_j\tau) = \frac{\partial}{\partial x_j}\left[\Gamma_{\rho_1} \frac{\partial\tau}{\partial x_j}\right] + 1 \tag{13}$$

In the ventilation of bored tunnels, the density of air is usually considered to be constant. Consider the equation of the conservation of mass

$$\frac{\partial u_j}{\partial x_j} = 0 \tag{14}$$

There is

$$u_j = \frac{\partial\tau}{\partial x_j} = \frac{\partial}{\partial x_j}\left[\Gamma_{\rho_1} \frac{\partial\tau}{\partial x_j}\right] + 1 \tag{15}$$

The form of the air-age distribution Eq. (13) is identical to the mass-diffusion equation with a source term of 1. The solution of the mass-diffusion equation is widely used in many computational fluid dynamic software packages. This makes it easy to solve the air-age distribution in a bored tunnel using existing numerical computation software.

Physical model

To ensure accurate simulation results, SOLIDWORKS was used to build a 1:1 physical model based on the site layout of the 5180 working faces of the Sanjiaohe coal mine, as shown in Fig. 1. The model includes a roadheader, transfer machine, dust fan, and belt conveyor; the roadway is a rectangle with 75.00 m × 6.30 m × 2.90 m area (length × width × height); the roadheader is an EBZ200T cantilever roadheader with 11.50 m length, 3.60 m width, and 1.90 m height; the belt conveyor (SSJ-1000) is 1.65 m from the right wall of the roadway; the wet screw dust fan (LZJC-III-B18.5) is on the roadheader, 1.65 m from the right side of the roadway. Furthermore, the dust suction port is connected to a 600-mm-diameter flexible air cylinder, which is fixed to the roadheader; the air inlet is located at the root of the cut-off

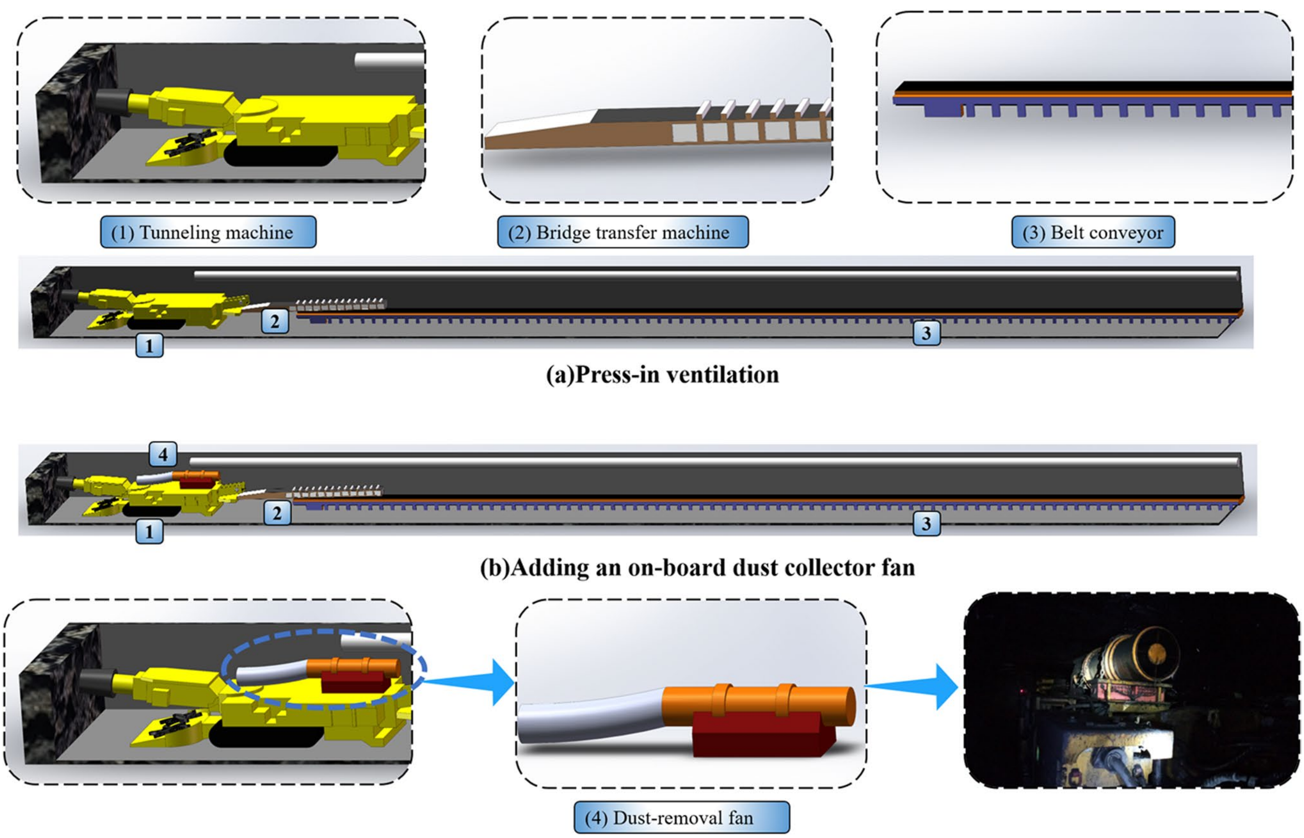

Fig. 1 Physical model

Sect. (5 m from the headway); the 600-mm-diameter flexible air cylinder is installed near the top of the roadway, 0.2 m from the right wall of the roadway; and the pressurized air outlet is 8 m from the face of the headway.

Mesh division and independence test

The Grid Convergence Index (GCI) proposed by P.J. Roache is the most common parameter used to evaluate the convergence of meshes (Lin et al. 2023; Nguyen and Chang 2021). At least three meshes with different densities are required to calculate the GCI. The sparsity of the mesh, dispersion result, and GCI are closely related (Volk et al. 2017). In general, the higher the mesh density is, the closer the discrete solution is to the exact solution, and, thus, the smaller the dispersion error and GCI are (Hefny and Ooka 2009; Mohamed et al. 2022). In this study, mesh convergence was quantitatively evaluated based on the GCI. The calculation procedure is as follows:

(1) Define a representative cell or the mesh size l for the calculation.

$$l = \left[\frac{1}{N}\sum_{i=1}^{N}\Delta v_i\right]^{1/3} \tag{16}$$

(2) Determine the key variable of the simulation with different meshing schemes. In this study, the diffusion of dust particles is mainly influenced by the airflow; thus, the air velocity v is the key variable.

(3) Evaluate the relative errors between the coarse and fine solutions of the key variables as follows:

$$\varepsilon = \left|\frac{v_{i,\mathrm{coarse}} - v_{i,\mathrm{fine}}}{v_{i,\mathrm{fine}}}\right| \tag{17}$$

(4) Calculate the root mean square of the relative error for sufficient points n in the critical region.

$$\varepsilon_{rms} = \left(\frac{\sum_{i=1}^{n}\varepsilon_1^2}{n}\right)^{1/2} \tag{18}$$

The GCI can be applied to fine mesh solutions.

$$\mathrm{GCI} = F\frac{\varepsilon_{rms}}{r^p - 1} \tag{19}$$

where $r=2$ and $p=2$; the safety factor $F=1.0$ is used to provide a GCI equivalent to the root mean square value ε_{rms}. Thus, the GCI represents a reduced version of ε_{rms} to account for refinement factors less than 2.

Meshing the established physical model (that of a scenario with press-in ventilation is taken as an example) results in four different meshes. They are ordered according to density: scheme I, scheme II, scheme III, and scheme IV (600,000 to 6 million cells). The mesh division scheme for the region of the tunneling machine is shown in Fig. 2. Dust diffusion in the tunnel is mainly affected by the airflow. Figure 2 compares the air velocities of different meshes. Meshes I–IV successfully simulate the airflow in the tunnel. Within 30 m from the working face, the air velocity varies greatly under different mesh schemes; behind 30 m from

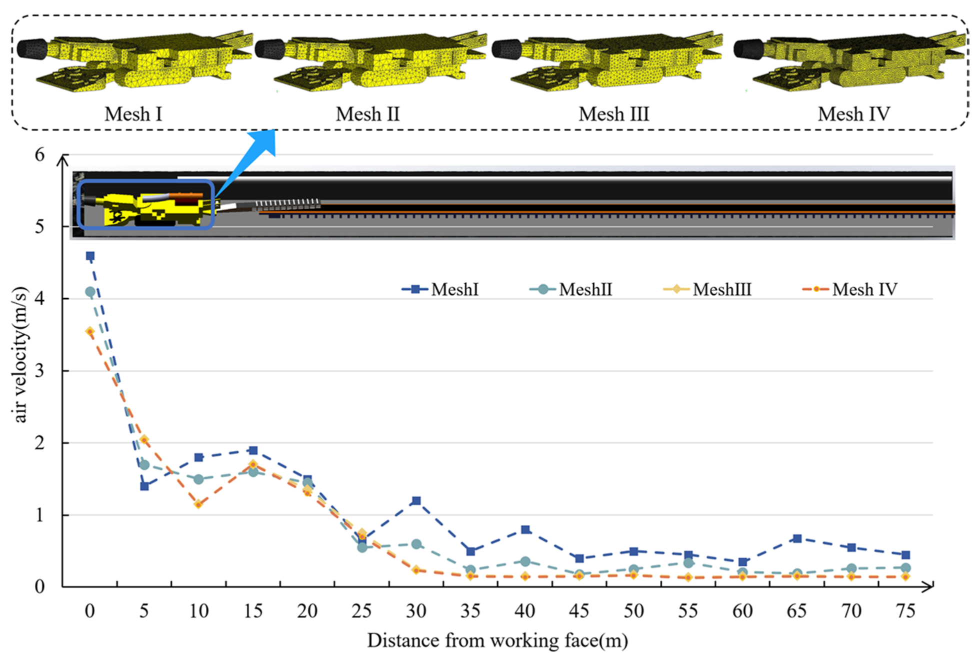

Fig. 2 Mesh situation and simulation results under different meshing schemes

the working face, the air velocity remains at 0.1–0.8 m/s. Evidently, the simulation results become more accurate with a better mesh quality. The air velocity near the roadheader decreases to 1.5–2 m/s for meshes I and II, whereas it is approximately 1.2 m/s for meshes III and IV. The lower quality of meshes I and II result in a large error in the calculation result of the airflow. Meshes III and IV result in very small errors, thereby indicating that the simulation results do not change with a reduction in the mesh parameters (i.e., the improvement of the mesh quality). The better quality of meshes III and IV results in more accurate airflow simulations. Hence, it can be assumed that the number of mesh points in this range results in mesh independence.

The details of the four meshes are shown in Table 1(a). By using the GCI calculation program, the GCI values were calculated for different air velocities v in the tunnel, as shown in Table 1(b). The results show that as the mesh becomes finer (and the mesh density increases), the air velocity v of ε_{rms} with the respective GCI decreases gradually. In general, the root mean square value ε_{rms} is less than 0.5%, and the GCI is less than 0.57% for a high-quality mesh. For meshes III and IV, ε_{rms} is lower than the standard specification, which means that the solution is mesh-independent. Finally, scheme III was selected because the simulation was more efficient in this case.

Setting of boundary conditions

The boundary conditions of the numerical simulation were adjusted to the actual conditions in the tunnel. The outlet of the pressurized air cylinder, the dust suction port of the on-board dust fan, and the exhaust port are the velocity inlets. The air velocity is positive because the outlet of the pressurized air cylinder and the exhaust of the on-board dust fan let air enter the tunnel. In addition, the air velocity is negative to represent the dust suction effect of the on-board dust fan inside the tunnel. The end of the tunnel is the pressure outlet; the front of the tunnel is the working face (i.e., the source of dust); the tunnel wall and equipment block the airflow to a certain extent and do not physically and chemically react with the dust; thus, they are considered non-slip solid wall surfaces, which are described with the standard wall function. The dust particles were characterized as follows: first, coal pieces were collected in the tunnel and crushed with a crusher; the particle size distribution of the coal dust was measured with a Mastersizer 3000 laser particle size analyzer (Fig. 3a) after sieving it through a 400 mesh sieve in a laboratory. The following assumptions were made for the numerical simulation: the flow field is an incompressible ideal gas, the tunnel flow field is isothermal, the heat transfer among objects is not considered, the dust particles are spherical, and interparticle interaction and cohesion are negligible. The boundary conditions and dust characteristics for the simulation are shown in Fig. 3b.

Table 1 Details and mesh convergence parameters of different mesh schemes

	Mesh scheme	Mesh		Min mesh spacing
		Cells	Vertexes	
a	Scheme I	600,000	105,350	0.29
	Scheme II	1,500,000	248,730	0.18
	Scheme III	4,000,000	554.150	0.12
	Scheme IV	6,000,000	1132.850	0.08
	Mesh size(× 104)	r	ε_{rms} (%)	GCI (%)
b	75–150	1.33	1.51	1.98
	150–300	1.33	0.34	0.44
	300–600	1.33	0.20	0.26

Numerical simulation results and analysis

The physical model was meshed with meshing scheme III and imported into ANSYS Fluent to simulate the airflow and dust migration in the tunnel. The resulting data were exported and post-processed with CFD-POST; the curves are the airflow trajectory, the arrows indicate the airflow direction, and the spheres represent the dust particle distribution. In addition, the rainbow column represents the airflow velocity and dust concentration.

Numerical simulation of scenario with press-in ventilation

Distribution of airflow field in tunnel with press-in ventilation

Figure 4 shows the overall and local distribution of the airflow in the tunnel with press-in ventilation.

According to Fig. 4

(1) The airflow field in the tunnel with press-in ventilation only can be roughly classified into a wall-attached jet area, a triangular jet area, a gyratory vortex area, a transitional airflow area, and a stable airflow area. The fresh airflow is ejected at the outlet of the pressurized air cylinder and transported to the working face in the form of a jet. The jet is affected by the coal wall and air, and its range gradually expands within 0–8 m distance from the working face, which results in a wall jet. During this period, the airflow energy decay is large; when the jet reaches the working face, the velocity has decreased to 2.22 m/s.
(2) After the jet has washed the working face, its direction changes owing to the blocking effect of the working face (such as at $Z = 0.5$ m in Fig. 5); most of the airflow

Fig. 3 Mastersizer 3000 laser particle size analyzer and boundary conditions for simulations

(a) Mastersizer 3000 laser particle size analyzer

Name	Type	Parameter
General	Solver type	Pressure-based
	Gravity	-9.81 m/s^2
	Temperature	288.16 K
Time	Windy	Steady
	Dust	Transient
Conditions of dust source	Dust source	Working face
	Particle size distribution of dust	Rosin–Rammler
	Median particle size of dust	2.32×10^{-5}
	Maximum particle size of dust	1.68×10^{-4}
	Minimum particle size of dust	6.04×10^{-7}

(b) Boundary conditions for CFD simulation

traces point downward and away from the pressurized air cylinder. Subsequently, it is blocked by the coal wall on the side away from the pressurized air cylinder and forms a triangular jet area at 0–10 m distance from the working face.

(3) Owing to the large width of the tunnel, a return airflow is not formed immediately; first, a lateral airflow that moves from the left to the right of the tunnel appears at the bottom of the tunnel. When the airflow reaches the right side of the tunnel, a transverse airflow moving from the right to the left side of the tunnel is formed in the upper part of the tunnel, as shown in the $Z=3$ m diagram; most of the airflow in the lower part moves to the right wall of the tunnel, and most of the airflow in the upper part moves to the left wall of the tunnel. At this time, the formed wind curtain controls the diffusion of dust to a certain extent.

(4) After the triangular jet area, the air velocity has decreased to 0.97 m/s. As shown in the $Z=11$ m diagram, the airflow moves to the side of the pressurized air cylinder, and the airflow traces mostly point to the back of the tunnel. Because the tunneling machine blocks some of the airflow, a vortex area is formed at 13–20 m distance from the working face.

(5) At 20–35 m distance from the working face, a transitional airflow field area is formed in which the concentrated airflow traces on the left side of the tunnel gradually expand and fill the whole tunnel width. As shown in the $Z=26$ m diagram, the airflow traces on the left side of the tunnel point toward the back of the tunnel, and the airflow traces on the right side of the tunnel are vortex-like and move gradually toward the back of the tunnel.

(6) At 35–75 m distance from the working face, a smooth airflow field has been formed (such as in the $Z=50$ m diagram); the airflow traces point toward the tunnel exit and are evenly distributed; in addition, the air velocity is constant (approximately 0.45 m/s).

Dust transport in tunnel with press-in ventilation

Figure 5 presents the simulated airflow distribution with discrete-phase dust particles at different times during tunnel boring under press-in ventilation. To visualize the dust migration, higher dust concentrations (> 200 mg/m^3) are highlighted.

According to Fig. 5

(1) Dust transport in the tunnel is mainly affected by the airflow and its own gravity; the former has a greater

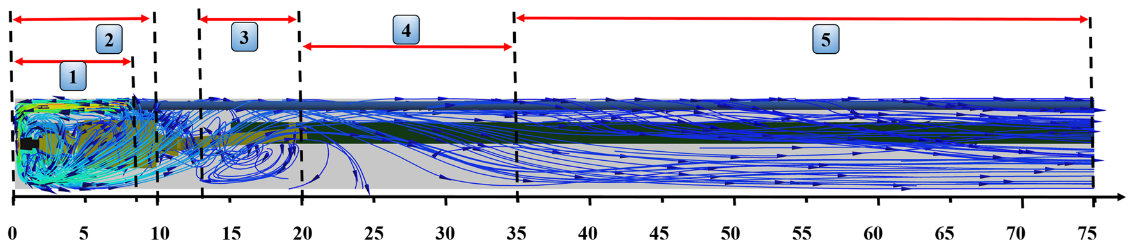

No.	Name of field	Distance from working face	No.	Name of field	Distance from working face
1	Wall jet area	0-8m	4	Transitional airflow field area	20-35m
2	Triangular jet area	0-10m	5	Smooth airflow field	35-75m
3	Vortex area	13-20m			

(a) Overall distribution of airflow under press-in ventilation

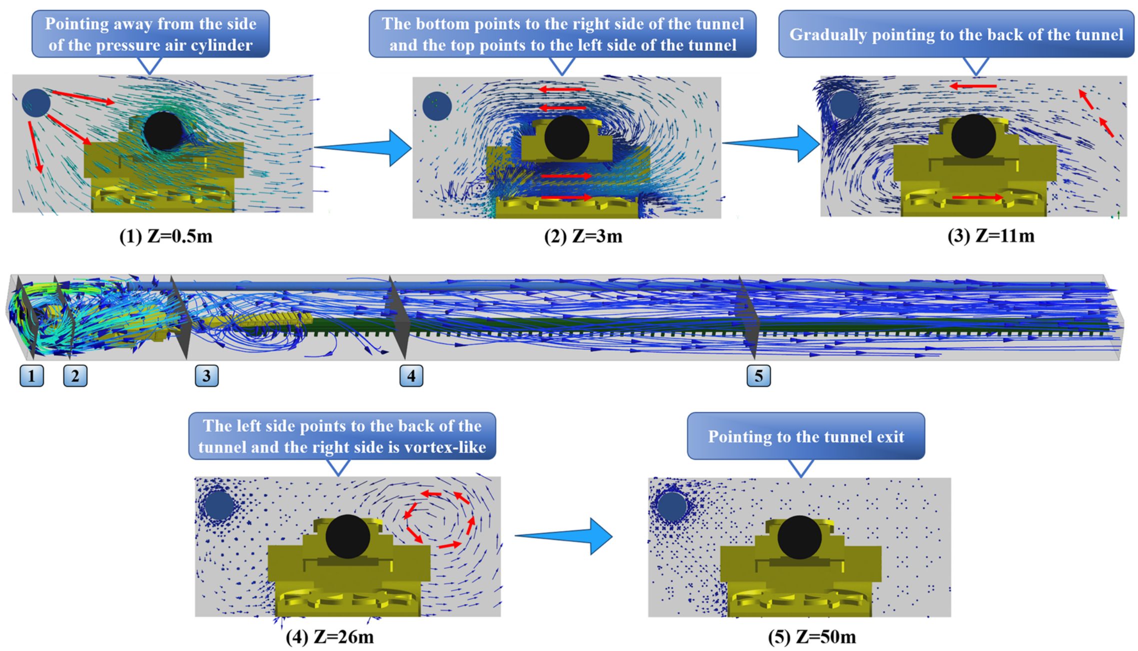

(b) Local distribution of airflow under pressure-in ventilation

Fig. 4 Distribution of airflow in tunnel with press-in ventilation

influence on dust transport. After coal dust has been generated at the working face, it is washed away by the airflow. At this time, the air velocity is high and can carry dust, which results in a dusty airflow that moves to the back of the tunnel. At $T=5$ s, the dust has spread to a 13 m distance from the working face.

(2) At $T=25$ s, the dust passes through the vortex airflow field at a 13–20 m distance from the working face. Owing to the weak dust-carrying capacity of the vortex airflow field and the tendency of large particles to settle down, more dust accumulates in the area of the vortex; thus, the dust concentration is higher in this area.

(3) Before $T=5$ s, the dust on the right side of the tunnel spreads faster than the dust on the left side; at $T=5$–85 s, the dust on the left side of the tunnel spreads faster than the dust on the right side; after $T=85$ s, the dust covers the whole tunnel section. Until $T=200$ s, the high and low dust concentrations spread to the end of the tunnel and filled the whole tunnel.

(4) With press-in ventilation, the diffusion trends of high and low dust concentrations are similar; they slowly move to the back of the tunnel under the effect of the airflow. The difference between their diffusion distances is not large. The transport equation for highly

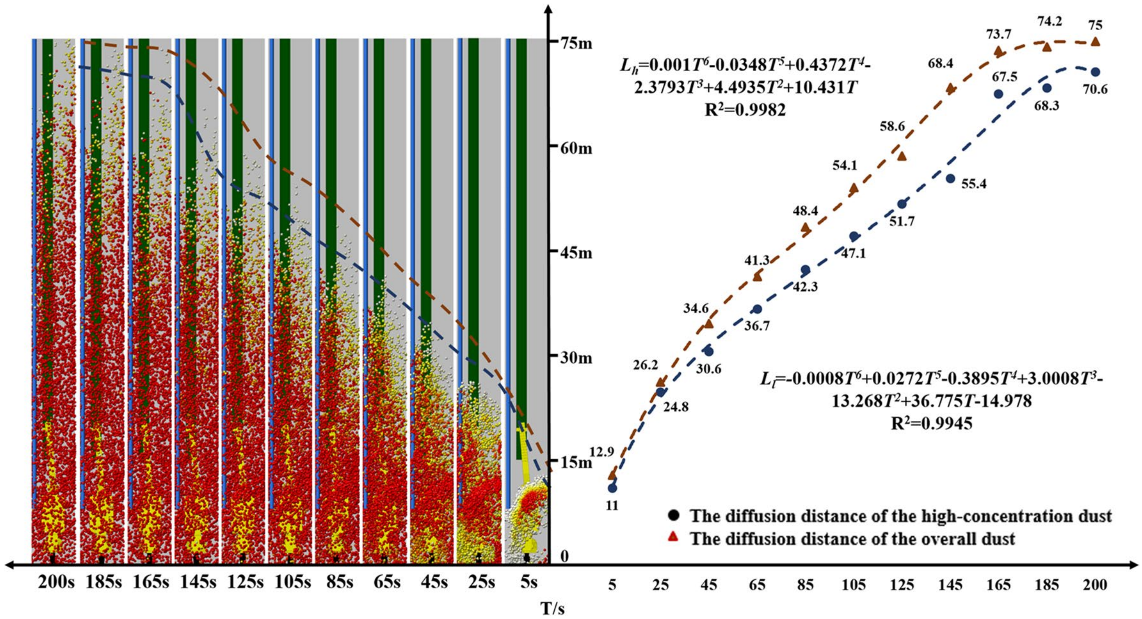

Fig. 5 Dust transport in tunnel with press-in ventilation

concentrated dust with respect to time was obtained by fitting:

$$L_h = 0.001T^6 - 0.0348T^5 + 0.4372T^4 \\ -2.3793T^3 + 4.4935T^2 + 10.431T$$

The transport equation for low-concentrated dust over time is as follows:

$$L_l = -0.0008T^6 + 0.0272T^5 + 0.43895T^4 \\ + 3.0008T^3 + 4.4935T^2 - 13.268T - 14.987$$

where L is the distance from the working face, m; and T is the time, s.

Numerical simulation analysis after the addition of dust removal fan

Airflow field in tunnel after addition of fan

In addition to press-in ventilation, on-board dust fans were used to study the resulting dust transport laws. Figure 6 shows the overall and local distribution of the airflow in the tunnel after the addition of the on-board dust collector.

According to Fig. 6

(1) After the addition of an on-board dust fan, the airflow field in the tunnel becomes more disordered. There are three more evident vortex areas in the tunnel.

(2) As shown in the $Z = 5$ m diagram, the airflow on both sides of the tunnel is simultaneously sucked in by the dust suction port of the dust fan, which creates multiple small vortices near the cutting section of the tunnel boring machine; the airflow on the return side is influenced by the airflow of the pressurized air cylinder, which results in a return airflow area at 0–8 m distance from the working face (see Vortex I in the diagram).

(3) As the dust fan is not connected to the exhaust pipe, the airflow from the exhaust of the dust fan sucks the airflow from the return side of the tunnel (see the $Z = 9$ m diagram); the airflow from the return side moves to the left side of the tunnel at 1.38 m/s. The negative pressure on the return side causes the airflow from the fan exhaust port to change its direction and move to the working face, thereby forming Vortex II within a 10–35 m distance from the working face. At $Z = 20$ m and 23 m (Fig. 6), the airflow moves to the working face or back of the tunnel; that is, at 9–30 m distance from the working face, a dust-controlling wind curtain of approximately 21 m length is created.

(4) Owing to the air-absorbing effect of the exhaust outlet and airflow of the pressurized air cylinder, the airflow near the pressurized air cylinder also forms a return flow in the direction from the top plate to the bottom plate of Vortex II. The remaining airflow is deflected to the return side with 0.16 m/s velocity behind $Z = 30$ m under the effect of Vortex II. When it reaches the left wall of the tunnel, an elliptical vortex is formed at 40–55 m distance from the working face under the

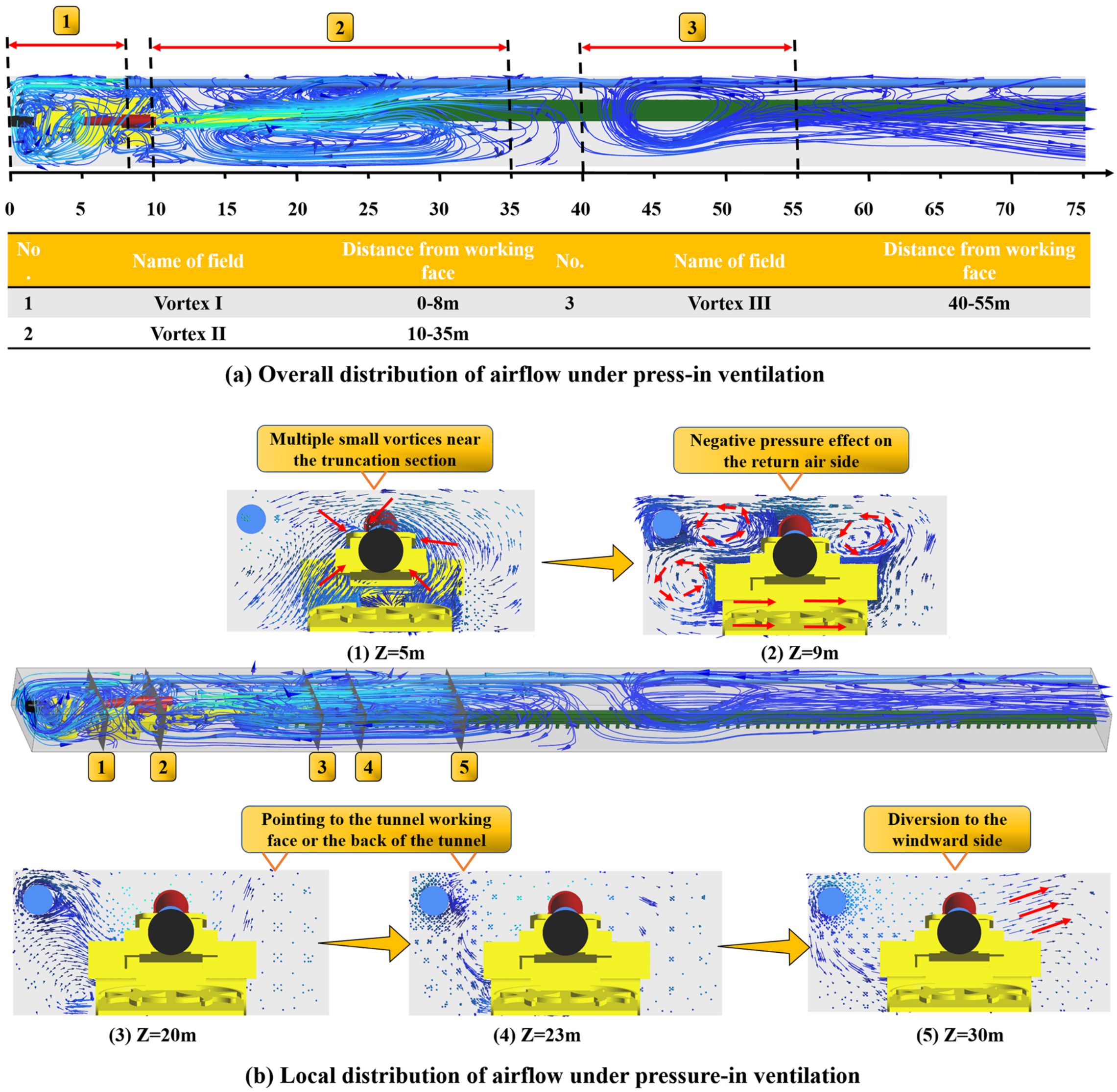

No.	Name of field	Distance from working face	No.	Name of field	Distance from working face
1	Vortex I	0-8m	3	Vortex III	40-55m
2	Vortex II	10-35m			

Fig. 6 Distribution of airflow in tunnel after the addition of an on-board dust fan

negative pressure of Vortex II, which is represented by Vortex III in the figure.

Dust transport in tunnel after the addition of fan

Figure 7 shows the transport of dust at different moments in the tunnel after the addition of the on-board dust fan. To visualize the dust migration, higher dust concentrations (> 200 mg/m^3) are highlighted.

According to Fig. 7

(1) Affected by Vortices I and II, the highly concentrated dust stays within $Z = 13$ m distance from the working face in the tunnel. The high-speed airflow at the outlet of the dust removal fan accelerates dust diffusion, and the dust particles spread to a point 75 m from the working face after 75 s of operation. In addition, the airflow from the outlet of the dust removal fan and the entrained airflow remove the dust that had accumulated near the working face. Subsequently, the dust accumulates on the right side of the tunnel (i.e., in the Vortex II area). When the dust on the right side of the tunnel reaches a certain concentration, it spreads to the Vortex III area and then migrates to the back of the tunnel.

(2) As the dust accumulates in the tunnel, the airflow changes. Vortex III moves toward the back of the tunnel, and the airflow traces become more evident. The distance between Vortex II and Vortex III increases, and that between Vortex III and the working face increases from 30 to 42 m. The dust accumulates between the two vortices and in Vortex III; thus, its concentration increases. Two hundred seconds after the start of the tunnel boring operation, the dust concentration on the left side of the tunnel is still low, with a significant difference from that on the right side. The

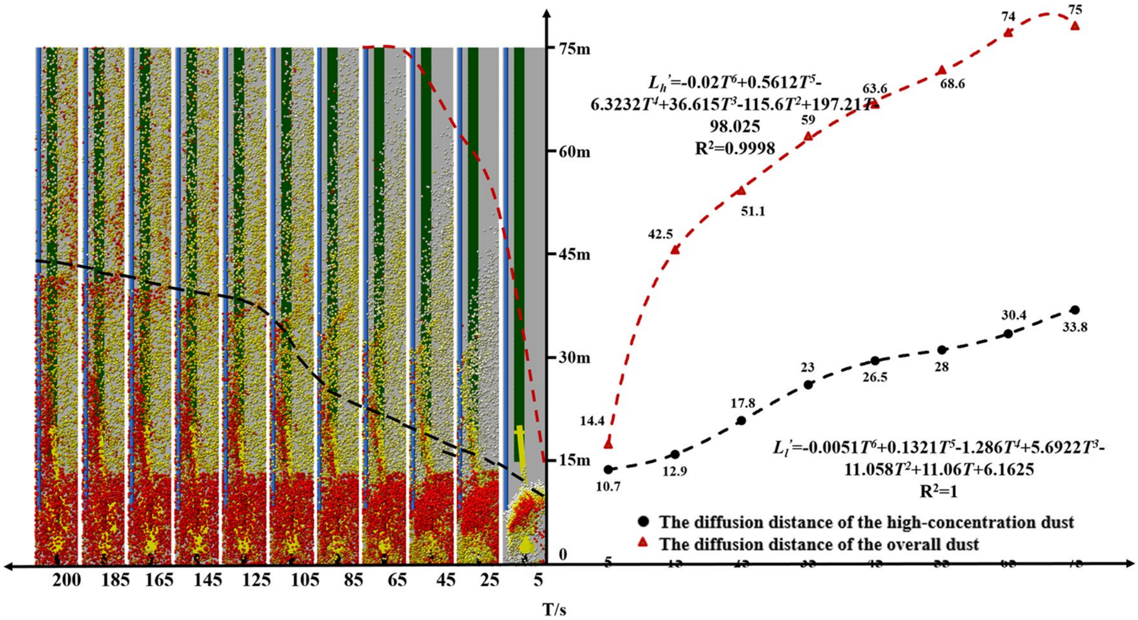

Fig. 7 Dust transport in tunnel after the addition of an on-board dust fan

dust settles down owing to the airflow and its own gravity; most of it settles down on the bottom plate. Compared to the results of press-in ventilation only, the air quality in the operation area was significantly improved after the addition of the dust fan.

(3) After the addition of the on-board dust fan, there is a clear difference between the diffusion trends of the high- and low-concentrated dust. Compared with the results of the scenario with press-in ventilation only, the dust concentration is effectively controlled owing to the addition of a dust fan. The equation for the transport of highly concentrated dust with respect to time was obtained by fitting:

$$L_h' = -0.02T^6 + 0.5612T^5 - 6.3232T^4 + 36.615T^3 + -115.6T^2 - 197.21T + 29.437 - 98.025$$

The equation for the transport of low-concentrated dust is as follows:

$$L_l' = -0.0051T^6 + 0.1321T^5 - 1.286T^4 + 5.6922^3 - 11.058T^2 + 11.06T + 3.1625$$

where L is the distance from the working face, m; and T is the time, s.

Simulation of change in the air age

Fresh air enters the tunnel through the pressurized air outlet, thereby constantly adding pollutants, which degrade the air quality. The shorter the air age, the fewer pollutants reach the location, which means that the ventilation system in the tunnel can discharge pollutants more effectively. To investigate the ability of the ventilation methods to remove pollutants and improve the air quality of the working environment, a comparative analysis of the air age under different ventilation methods was carried out, where the indicator "air age" is limited to a gaseous tracer.

The UDF program was used to build the UDS air age numerical calculation solver and import it into Fluent to analyze the air age distribution through numerical simulations. To calculate the mean air age in a tunnel, the convective diffusion equation must be added, which can be solved for a specific MMA with a custom scalar ϕ_i (i.e., the air age) (Buratti et al. 2011; Ning et al. 2016; Park et al. 2018; Yi et al. 2020):

$$\frac{\partial \rho \phi_i}{\partial t} - \nabla\left(\Gamma_i \nabla \phi_i\right) = S_{\phi_i} \tag{20}$$

$$\Gamma_i = 2.88 \times 10^{-5}\rho + \frac{\mu_{eff}}{0.7 \neq} \tag{21}$$

Where Γ_i is the diffusion coefficient of the air age, $S_{\phi i}$ is the source term of the air age, and μ_{eff} s the effective air viscosity.

Air age distribution of press-in ventilation mode

Figure 8 shows the air age distribution in the tunnel with press-in ventilation. According to the results.

(1) With press-in ventilation, the fresh airflow from the pressurized air cylinder has a major effect on the airflow in the tunnel. According to Fig. 8a, close to the working face, the fresh airflow has more influence on the air in the upper part of the tunnel; the air ages between the boring machine and belt conveyor and bottom plate reached more than 80 and 600 s, respectively; the air in this area is not easily renewed.
(2) At 20 m distance from the working face, the airflow on the return side moves to the pressure side owing to the influence of the vortex; the air age on the return side reaches 120 s, which is 70% longer than the time required to reach the pressure side. Figure 8a presents the air age distribution at 30 to 70 m distance from the working face; the airflow on the right side of the tunnel spreads to the left side of the tunnel; the closer it is to the back of the tunnel, the weaker is the interference with the airflow near the pressurized air cylinder.
(3) According to Fig. 8b, in the $Y=2.3$ m section, the fresh airflow can travel 38 m from the working face within 140 s; in the $Y=1.55$ m section, it can travel 37 m from the working face within 140 s; that is, the fresh airflow has a greater influence on the air near the roof of the tunnel. Behind 55 m from the working face, the airflow does almost not interfere with the air near the windpipe, and the air age exceeds 700 s. Once the dust has entered the area, it accumulates and cannot be easily removed.

Air age distribution after addition of dust fan

Figure 9 illustrates the air age distribution in the tunnel with an on-board dust extractor fan.

(1) According to Fig. 9a, the fresh airflow only affects the airflow near the pressurized air outlet and the suction air outlet of the dust fan because the dust fan rapidly extracts the pressed-in fresh airflow. The airflow around the roadheader at $Z=5$ m is only disturbed very slightly by the airflow, and the air age reaches more than 90 s at some points. After the airflow has been discharged at high speed from the exhaust of the dust fan, it will approach the roadheader again under the action of Vortex II; the air age near the roadheader reaches a maximum of 114.4 s at $Z=10$ m.

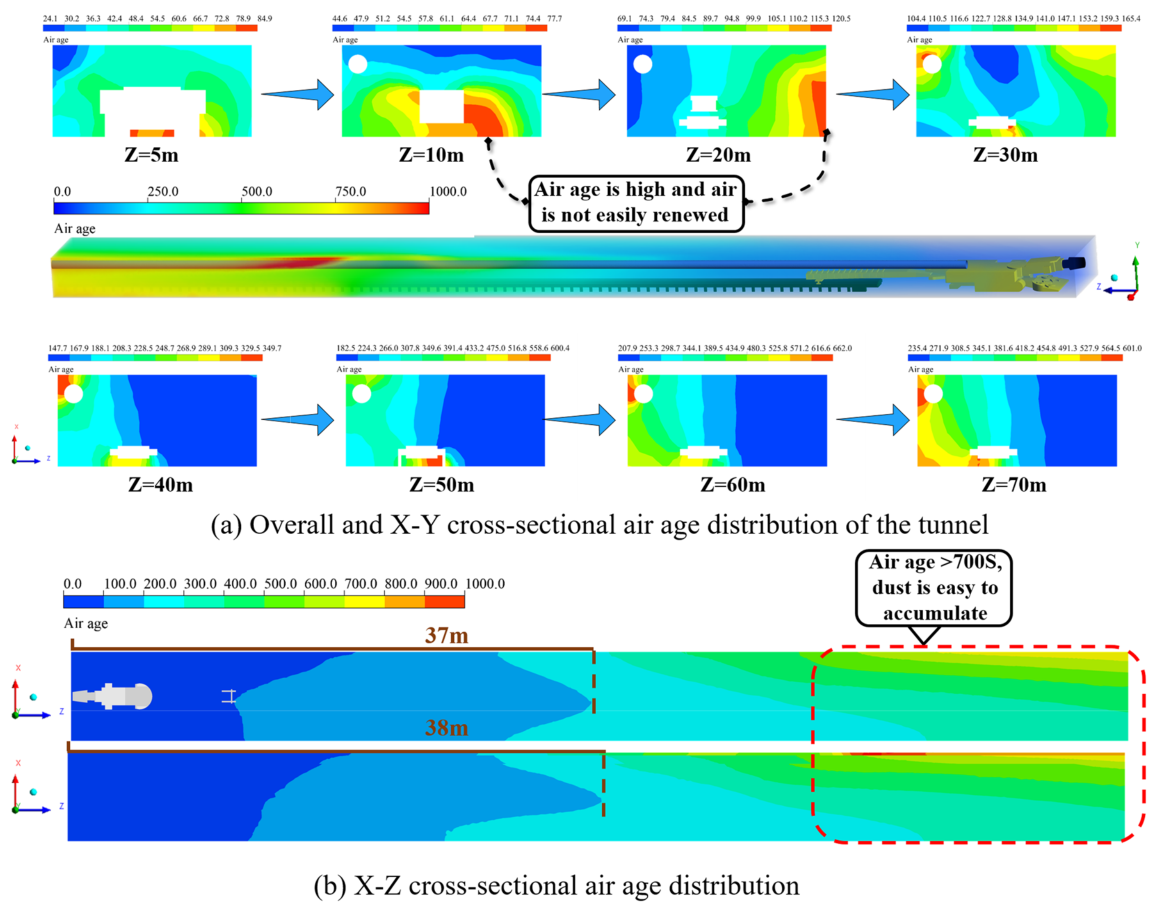

Fig. 8 Air age distribution in tunnel with press-in ventilation

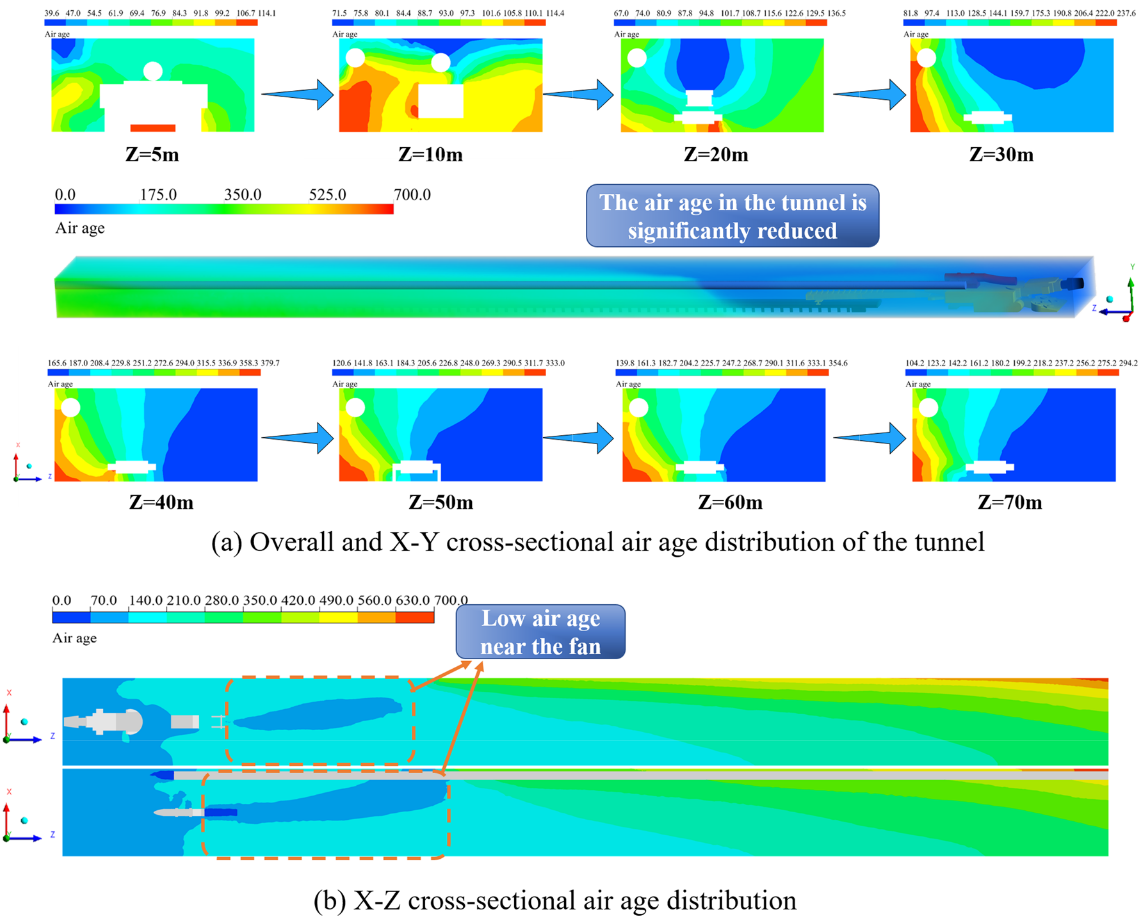

Fig. 9 Air age distribution in tunnel after the addition of an on-board dust fan

(2) At 30–70 m distance from the working face, the high-speed airflow from the exhaust air outlet reduces the overall air age in the tunnel. The maximum air age exceeds 660 s in the cross-section of the press-in ventilation mode, and it can reach 379 s in the cross-section after the addition of the dust fan. The air on the left side of the tunnel (i.e., the area of the workers) is renewed, and the air age is much shorter than that on the right side of the tunnel; thus, the air quality is improved in this area.

(3) According to Fig. 9b, only the air age near the outlet of the pressurized air cylinder and the exhaust of the dust fan is shorter than 40 s; the fresh airflow can move up to 66 m from the working face within 160 s at $Y = 1.55$ m and 2.3 m. According to the air age contour diagram, the airflow from the on-board dust fan moves to the side of the pressurized air cylinder and then to the left wall of the tunnel after reaching the Vortex II area.

Comparison of air age distributions of two ventilation methods

Measurement point A (i.e., the worker's position) and measurement point B (i.e., the pressurized air side) on each *X*–*Y* plane were selected for comparison; Fig. 10 compares the air age at measurement points A and B under the two ventilation methods.

(1) The maximum air age in the press-in ventilation mode is 747.3 s, while it is only 431.5 s after the addition of a dust fan. In the area up to 10 m from the working face, the air age is below 78 s with press-in ventilation. After the addition of the dust fan, there are areas in the tunnel where the air age exceeds 78 s; after changing the ventilation method, the air age in the tunnel is evidently shortened, and the air quality near the rear air duct of the tunnel The situation where the air age exceeded 700 s was also improved. The discharge capacity has been increased, which ensures that the operators breathe fresher air while controlling the dust spread.

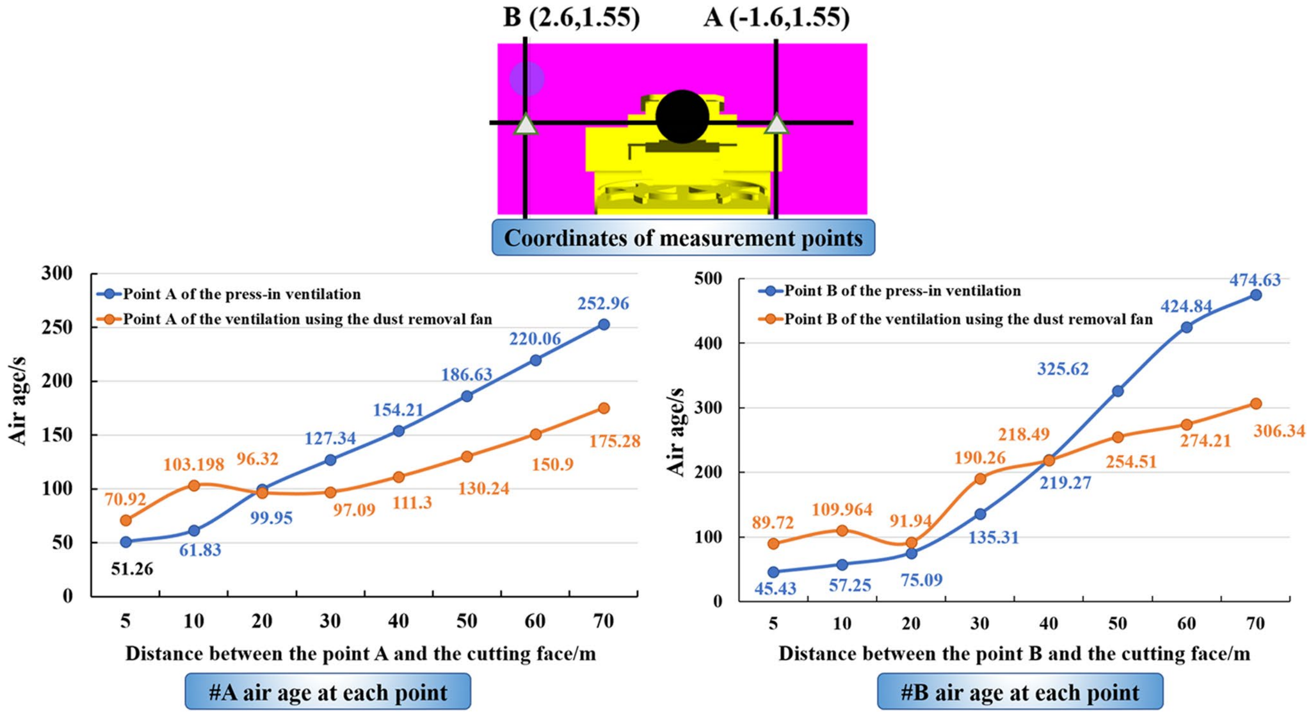

Fig. 10 Comparison of air ages of two ventilation modes

(2) According to the scatter diagram of the air ages at points A and B of each section, the change in the air age tends to be smoother after the addition of a dust fan. In addition, the difference in the air ages decreases with increasing distance from the working face. The air age at point A can be reduced by up to 31.4%, and that at point B can be decreased by up to 35.5%. The air ages at the two points near the working face are longer after the installation of the dust fan, and the diffusion of the airflow is more limited, which helps to control the dust near the working face and prevents the dust from spreading in the whole tunnel.

Automatic wind-mist synergistic wet high-frequency oscillation dust-capturing technology for coal mine tunnel

The results of this study show that the addition of an on-board dust fan reduces coal dust pollution in a tunnel to a certain extent compared to the use of press-in ventilation only; however, the coal dust still spreads throughout the tunnel. Therefore, spraying measures must be added to dust control with wind curtains and dust removal with on-board dust fans. Considering the atomization angle, effective range, and other macroscopic atomization characteristics of a fog field at different spray pressures, we finally chose a wide-angle solid conical nozzle.

Based on the dust diffusion results in the tunnel with press-in ventilation and an on-board dust fan, a wet high-frequency oscillation dust-capturing net device was developed; it mainly consists of an equipment frame, a high-frequency oscillation net, spray device, removable base, and infrared sensors. Figure 11 shows a schematic of the wet high-frequency oscillation dust-capturing net device for coal mine tunnels.

This device is located between the tunnel transfer machine and the transport machine. In addition, a high-density high-frequency oscillating net is installed inside the frame of the device. When the dusty air flows through the high-frequency oscillating net without being purified by the on-board dust removal fan, the spraying system creates a water film with a strong dust-suppressing effect on the surface of the high-frequency oscillating net. Universal wheels are installed at the bottom of the device to facilitate its movement. Moreover, there is a door at the bottom right of the device so that pedestrians can enter it. There are infrared sensors at the front and rear of the device. When they detect a pedestrian, they automatically turn off the spraying system. According to the field application, the wet high-frequency oscillation dust-capturing device can effectively capture dusty airflow with an on-board dust fan, improve the air quality in a highly polluted tunnel, and ensure clean production during tunnel boring.

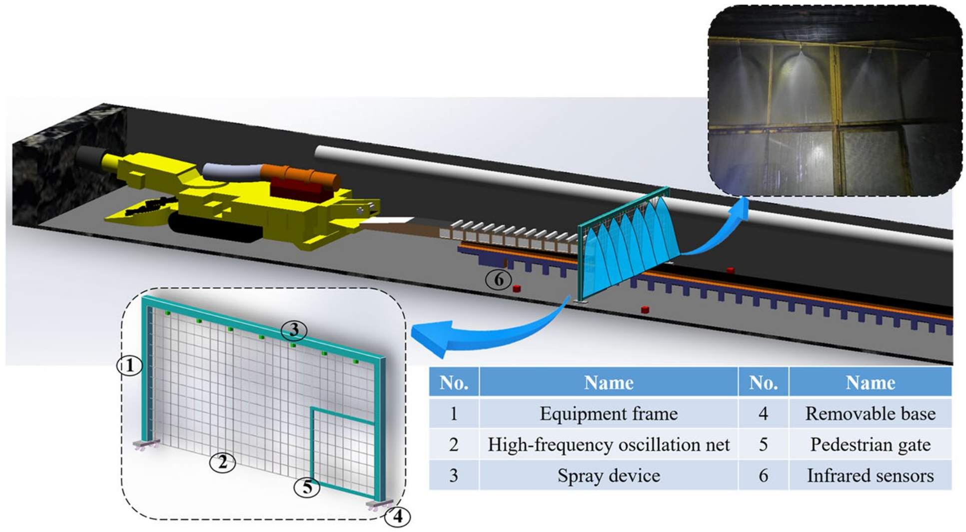

No.	Name	No.	Name
1	Equipment frame	4	Removable base
2	High-frequency oscillation net	5	Pedestrian gate
3	Spray device	6	Infrared sensors

Fig. 11 Schematic of wet high-frequency oscillation dust-capturing device for coal mine tunnels

Discussion

In this study, the spatiotemporal evolution law of dust pollution under different ventilation modes in a typical bored tunnel was investigated, and air age was innovatively introduced as an index for evaluating tunnel air quality. We found that the dust removal effect was clear, and the air age was considerably reduced after the addition of a dust removal fan. We also developed an automated wind-mist synergistic wet high-frequency oscillation dust-capturing technology for tunnel boring, which notably improved the problem of high levels of coal dust pollution in tunnels. It is worth noting that, although the size of the closed area is different in different restricted spaces, the main transportation trajectory of wind flow and dust in a closed area remains unchanged, so the main conclusions obtained in our study are also applicable to other cross-section tunnels. Although the tunneling equipment and operating conditions are different in different tunnels, the differences in tunneling equipment have little effect on coal mine tunnels that are hundreds or thousands of meters long. Moreover, all other mechanical equipment in such tunnels is similar, and this mechanical equipment has a similar effect on the wind flow field and dust transportation. So, the underlying physical principles outlined in our study are generalizable. However, this study involved few ventilation parameters, and therefore the analysis of the dust control effect and its sensitivity under different ventilation parameters must be investigated further. The dust distribution law of different particle sizes in a tunnel also needs to be explored in depth. This will inform our future research direction. At the same time, we will study the diffusion and deposition of dust particles in human lungs, and we will make suggestions for the development of appropriate occupational health-protection equipment.

Conclusions

(1) In the tunnel with press-in ventilation only, a triangular vortex area appears near the working face; driven by the airflow, the dust slowly spreads to the tunnel exit (which is 75 m from the working face), and the dust concentration in the tunnel exceeds 200 mg/m^3 after 200 s. After the addition of a dust fan, the two vortex areas are increased, and an effective dust-controlling wind curtain is formed. The dust basically stays within the area 13 m from the working face, whereas the dust at the back of the tunnel generally accumulates in the bottom plate. Thus, the dust dispersion is controlled to a certain extent.

(2) The coal dust concentration is severe under press-in ventilation only. It can be decreased to a certain extent by the addition of an on-board dust fan. The dust fan increases the airflow velocity in the tunnel and significantly decreases the air age in the tunnel. The air on the left side of the tunnel is constantly renewed by the high-pressure airflow from the dust fan exhaust; the maximum air age at the left measurement point can be reduced by 34.1%. The resulting air age is only 431.5 s; thus, the workers can breathe fresh air.

(3) In addition to dust control with a wind curtain and dust fan, an automated wind-mist synergistic wet high-frequency oscillation dust-capturing technology for coal mine tunnels was developed. It effectively reduces high coal dust concentrations in the tunnel, thus reducing the abrasive effect of coal dust on the mechanical equipment and the health hazard to operators. The resulting operation process is clean, safe, and efficient.

(4) The presented study still has some deficiencies. First, the coal dust concentrations must be analyzed at different ventilation parameters, and the effect of different

ventilation parameters on the dust control result must be studied more thoroughly. Second, the pollution effect of respirable dust generated during tunnel boring still lacks in-depth investigation. In the future, we will thoroughly study the diffusion laws of dust with different particle sizes. Moreover, we will study the diffusion and deposition of dust particles in human lungs and develop health protection equipment.

Author contribution All authors contributed to the study conception and design. Material preparation, data collection, and analysis were performed by Wen Nie, Chenwang Jiang, and Ning Sun. Assist in numerical simulation, field investigation, and validation were performed by Lidian Guo, Qiang Liu, Chengyi Liu, and Wenjin Niu. The first draft of the manuscript was written by Chenwang Jiang and Ning Sun, and all authors commented on previous versions of the manuscript. All authors read and approved the final manuscript.

Funding This work has been funded by the National Natural Science Foundation of China (NO. 52174191 and 51874191), the National Key R&D Program of China (2017YFC0805201), the Qingchuang Science and Technology Project of Shandong Province University (2020KJD002), and the Taishan Scholars Project Special Funding (TS20190935).

Data availability All data generated or analyzed during this study are included in this published article (and its supplementary information files).

Declarations

Ethics approval and consent to participate Not applicable.

Consent for publication Not applicable.

Competing interests The authors declare no competing interests.

References

Azam S, Mishra DP (2019) Effects of particle size, dust concentration and dust-dispersion-air pressure on rock dust inertant requirement for coal dust explosion suppression in underground coal mines. Process Saf Environ Prot 126:35–43. https://doi.org/10.1016/j.psep.2019.03.030

Bayatian M, Azari MR, Ashrafi K, Jafari MJ, Mehrabi Y (2021) CFD simulation for dispersion of benzene at a petroleum refinery in diverse atmospheric conditions. Environ Sci Pollut Res Int. https://doi.org/10.1007/s11356-020-12254-1

Buratti C, Mariani R, Moretti E (2011) Mean age of air in a naturally ventilated office: experimental data and simulations. Energy and Buildings 43:2021–2027. https://doi.org/10.1016/j.enbuild.2011.04.015

Calautit JK, Hughes BR (2014) Measurement and prediction of the indoor airflow in a room ventilated with a commercial wind tower. Energy and Buildings 84:367–377. https://doi.org/10.1016/j.enbuild.2014.08.015

Chang P, Xu G, Huang J (2020) Numerical study on DPM dispersion and distribution in an underground development face based on dynamic mesh. Int J Min Sci Technol 30:471–475. https://doi.org/10.1016/j.ijmst.2020.05.005

de Medeiros Lima SV, Padoin N, Soares C (2021) CFD analysis of a H(2)O(2)/UVC water treatment process in the annular FluHelik reactor. Environ Sci Pollut Res Int 28:41224–41232. https://doi.org/10.1007/s11356-021-13566-6

Ding Y, Huang B, Wu C, He Q, Lu K (2019) Kinetic model and parameters study of lignocellulosic biomass oxidative pyrolysis. Energy 181:11–17. https://doi.org/10.1016/j.energy.2019.05.148

Feng L, Hao H, Wang K (2022) Study on pressure relief and reset technology and dynamicresponse law of mine shaft explosion-proof covers. J Shandong Univ Sci Technol (Nat Sci) 03:50–7. https://doi.org/10.16452/j.cnki.sdkjzk.2022.03.006

Hefny MM, Ooka R (2009) CFD analysis of pollutant dispersion around buildings: effect of cell geometry. Build Environ 44:1699–1706. https://doi.org/10.1016/j.buildenv.2008.11.010

Hongchao X, Guanhua N, Shang L, Qian S, Kai D, Jingna X, Gang W, Yixin L (2019) The influence of surfactant on pore fractal characteristics of composite acidized coal. Fuel 253:741–753. https://doi.org/10.1016/j.fuel.2019.05.073

Hormigos-Jimenez S, Padilla-Marcos MA, Meiss A, Gonzalez-Lezcano RA, Feijó-MuÑoz J (2018) Experimental validation of the age-of-the-air CFD analysis: a case study. Science and Technology for the Built Environment 24:994–1003. https://doi.org/10.1080/23744731.2018.1444885

Hu S, Chen Y, Hao Y, Chen Z, Feng G, Li G, Guan S, Zhang X, Li S (2020) Experimental study of the effects of fine retention on fracturing proppant permeability in coalbed methane reservoirs. J Nat Gas Sci Eng 83:103604. https://doi.org/10.1016/j.jngse.2020.103604

Korkmaz KB, Werner S, Bensow R (2021) Verification and validation of CFD based form factors as a combined CFD/EFD method. J Mar Sci Eng 9:9010075. https://doi.org/10.3390/jmse9010075

Kwon KS, Lee IB, Han HT, Shin CY, Hwang HS, Hong SW, Bitog JP, Seo IH, Han CP (2011) Analysing ventilation efficiency in a test chamber using age-of-air concept and CFD technology. Biosys Eng 110:421–433. https://doi.org/10.1016/j.biosystemseng.2011.08.013

Laín S, Sommerfeld M (2012) Numerical calculation of pneumatic conveying in horizontal channels and pipes: detailed analysis of conveying behaviour. Int J Multiph Flow 39:105–120. https://doi.org/10.1016/j.ijmultiphaseflow.2011.09.006

Li Y, Wang P, Liu R, Jiang Y, Han H (2020) Determination of the optimal axial-to-radial flow ratio of the wall-mounted swirling ventilation in fully mechanized excavation face. Powder Technol 360:890–910. https://doi.org/10.1016/j.powtec.2019.10.067

Li Z, Ren T, Li X, Cheng Y, He X, Lin J, Qiao M, Yang X (2023) Full-scale pore structure characterization of different rank coals and its impact on gas adsorption capacity: a theoretical model and experimental study. Energy 277:127621. https://doi.org/10.1016/j.energy.2023.127621

Lin C, Ooka R, Kikumoto H, Flageul C, Kim Y, Wang Y, Maison A, Zhang Y, Sartelet K (2023) Large-eddy simulations on pollutant reduction effects of road-center hedge and solid barriers in an idealized street canyon. Build Environ 241:110464. https://doi.org/10.1016/j.buildenv.2023.110464

Liu Q, Wang Q, Wu P, Wang JX, Lv XJ (2022) Research progress in application of red mud in cementitious mater.J Shandong Univ Sci Technol (Nat Sci) 41(03):66–74. https://doi.org/10.16452/j.cnki.sdkjzk.2022.03.008

Lu XX, Wang CY, Xing Y, Shen C, Shi GY (2021) Investigation on the dust migration behavior and safety zone in the fully mechanized mining face. Environ Sci Pollut Res Int 28:20375–20392. https://doi.org/10.1007/s11356-020-12050-x

Mo J, Yang J, Ma W, Chen F, Zhang S (2020) Numerical simulation and field experiment study on onboard dust removal technology based on airflow-dust pollution dispersion characteristics. Environ Sci Pollut Res Int 27:1721–1733. https://doi.org/10.1177/01445987211055807
Mohamed MA, Afgan I, Salim MH, Mohamed IK (2022) Low speed aerodynamic characteristics of non-slender delta wing at low angles of attack. Alex Eng J 61:9427–9435. https://doi.org/10.1016/j.aej.2022.03.003
Morozova N, Trias FX, Capdevila R, Schillaci E, Oliva A (2022) A CFD-based surrogate model for predicting flow parameters in a ventilated room using sensor readings. Energy Build 266:112146. https://doi.org/10.1016/j.enbuild.2022.112146
Nguyen KH, Chang K (2021) Large eddy simulation of turbulent heat transfer in pipe using NEK5000 based on the spectral element method and uncertainty quantification by GCI estimation. Int J Compust Fluid Dynamics 35:210–223. https://doi.org/10.1080/10618562.2021.1926999
Nie W, Guo L, Yu H, Liu Q, Hua Y, Xue Q, Sun N (2022) Study on dust-gas coupling pollution law and selection of optimal purification distance of air duct during tunneling process. Environ Sci Pollut Res Int 29:74097–74117. https://doi.org/10.1007/s11356-022-20995-4
Ning M, Mengjie S, Mingyin C, Dongmei P, Shiming D (2016) Computational fluid dynamics (CFD) modelling of air flow field, mean age of air and CO2 distributions inside a bedroom with different heights of conditioned air supply outlet. Appl Energy 164:906–915. https://doi.org/10.1016/j.apenergy.2015.10.096
Park J, Jo Y, Park G (2018) Flow characteristics of fresh air discharged from a ventilation duct for mine ventilation. J Mech Sci Technol 32:1187–1194. https://doi.org/10.1007/s12206-018-0222-9
Rahimi S, Ataee-pour M, Madani H, Aminossadati SM (2021) Investigating the impact of gas emission uncertainty on airflow distribution in an auxiliary ventilation system using CFD and Monte-Carlo simulation. Build Environ 204:108165. https://doi.org/10.1016/j.buildenv.2021.108165
Sajjadi H, Tavakoli B, Ahmadi G, Dhaniyala S, Harner T, Holsen TM (2016) Computational fluid dynamics (CFD) simulation of a newly designed passive particle sampler. Environ Pollut 214:410–418. https://doi.org/10.1016/j.envpol.2016.04.020
Sun D, Shi X, Zhang Y, Zhang L (2021) Spatiotemporal distribution of traffic emission based on wind tunnel experiment and computational fluid dynamics (CFD) simulation. J Clean Prod 282:124495. https://doi.org/10.1016/j.jclepro.2020.124495
Toraño J, Torno S, Menéndez M, Gent M (2011) Auxiliary ventilation in mining roadways driven with roadheaders: validated CFD modelling of dust behaviour. Tunn Undergr Space Technol 26:201–210. https://doi.org/10.1016/j.tust.2010.07.005
Tretiakow D, Tesch K, Skorek A (2021) Mitigation effect of face shield to reduce SARS-CoV-2 airborne transmission risk: preliminary simulations based on computed tomography. Environ Res 198:111229. https://doi.org/10.1016/j.envres.2021.111229
Volk A, Ghia U, Stoltz C (2017) Effect of grid type and refinement method on CFD-DEM solution trend with grid size. Powder Technol 311:137–146. https://doi.org/10.1016/j.powtec.2017.01.088
Wang H, Nie W, Cheng W, Liu Q, Jin H (2018) Effects of air volume ratio parameters on air curtain dust suppression in a rock tunnel's fully-mechanized working face. Adv Powder Technol 29:230–244. https://doi.org/10.1016/j.apt.2017.11.007
Wang Z, Li S, Ren T, Wu J, Lin H, Shuang H (2019) Respirable dust pollution characteristics within an underground heading face driven with continuous miner – a CFD modelling approach. J Clean Prod 217:267–283. https://doi.org/10.1016/j.jclepro.2019.01.273
Wang P, Gao R, Liu R, Yang F (2020) CFD-based optimization of the installation location of the wall-mounted air duct in a fully mechanized excavation face. Process Saf Environ Prot 141:234–245. https://doi.org/10.1016/j.psep.2020.04.049
Wang H, Liu B, Liu X, Lu C, Deng J, You Z (2021) Dispersion of carbon dioxide released from buried high-pressure pipeline over complex terrain. Environ Sci Pollut Res Int 28:6635–6648. https://doi.org/10.1007/s11356-020-11012-7
Xiao P, Yu H, Wang D, Zhao X, Li C, Zhao B et al (2022) Technology and application ofactive support replacing passive support in advance section of backfill mining. J Shandong Univ Sci Technol (Nat Sci) 41(03):41–49. https://doi.org/10.16452/j.cnki.sdkjzk.2022.03.005
Xie Y, Cheng W, Yu H, Sun B (2018) Microscale dispersion behaviors of dust particles during coal cutting at large-height mining face. Environ Sci Pollut Res Int 25:27141–27154. https://doi.org/10.1007/s11356-018-2735-2
Xu Q, Peng S, Xu J, Jiao F, Cheng L, Jia L, Yang H, Yang Y, Liu R, Ramakrishna S (2023) Study on time effect of acidified pulverized coal micro components and discussion on mathematical correlation of influencing factors. Fuel 342:127842. https://doi.org/10.1016/j.fuel.2023.127842
Yang L, Ye M, He BJ (2014) CFD simulation research on residential indoor air quality. Sci Total Environ 472:1137–1144. https://doi.org/10.1016/j.scitotenv.2013.11.118
Yi H, Park J, Kim MS (2020) Characteristics of mine ventilation air flow using both blowing and exhaust ducts at the mining face. J Mech Sci Technol 34:1167–1174. https://doi.org/10.1007/s12206-020-0218-0
Yuce BE, Nielsen PV, Wargocki P (2022) The use of Taguchi, ANOVA, and GRA methods to optimize CFD analyses of ventilation performance in buildings. Build Environ 225:109587. https://doi.org/10.1016/j.buildenv.2022.109587
Zhang K, Zhang J, Wei J, Ren T, Xu X (2019) Coal seam water infusion for dust control: a technical review. Environ Sci Pollut Res Int 26:4537–4554. https://doi.org/10.1007/s11356-018-04086-x
Zhang C, Yuan S, Zhang N, Li C, Li H, Yang W (2021) Dust-suppression and cooling effects of spray system installed between hydraulic supports in fully mechanized coal-mining face. Build Environ 204:108106. https://doi.org/10.1016/j.buildenv.2021.108106
Zhuo B, Zhu M, Fang Y, Wang F, Yao Y, Li S (2021) Numerical and experimental analyses for rubber-sand particle mixtures applied in high-filled cut-and-cover tunnels. Construct Build Mater 306:124874. https://doi.org/10.1016/j.conbuildmat.2021.124874